Dynamic Contrast-enhanced MR Imaging of Carotid Atherosclerotic Plaque: Model Selection, Reproducibility, and Validation.

Dynamic Contrast-enhanced MR Imaging of Carotid Atherosclerotic Plaque: Model Selection, Reproducibility, and Validation[1]

Michaela E. Gaens, MSc
Walter H. Backes, PhD
Stefan Rozel, MSc
Matthijs Lipperts, MSc
Stefan N. Sanders, BSc
Karolien Jaspers, MSc
Jacques P. M. Cleutjens, PhD
Judith C. Sluimer, PhD
Sylvia Heeneman, PhD
Mat J. A. P. Daemen, MD, PhD
Rob J. T. J. Welten, MD, PhD
Jan-Willem H. Daemen, MD, PhD
Joachim E. Wildberger, MD
Robert M. Kwee, MD, PhD
M. Eline Kooi, PhD

Purpose: To compare four known pharmacokinetic models for their ability to describe dynamic contrast material–enhanced magnetic resonance (MR) imaging of carotid atherosclerotic plaques, to determine reproducibility, and to validate the results with histologic findings.

Materials and Methods: The study was approved by the institutional medical ethics committee. Written informed consent was obtained from all patients. Forty-five patients with 30%–99% carotid stenosis underwent dynamic contrast-enhanced MR imaging. Plaque enhancement was measured at 16 time points at approximately 25-second image intervals by using a gadolinium-based contrast material. Pharmacokinetic parameters (volume transfer constant, K^{trans}; extracellular extravascular volume fraction, v_e; and blood plasma fraction, v_p) were determined by fitting a two-compartment model to plaque and blood gadolinium concentration curves. The relative fit errors and parameter uncertainties were determined to find the most suitable model. Sixteen patients underwent imaging twice to determine reproducibility. Carotid endarterectomy specimens from 16 patients who were scheduled for surgery were collected for histologic validation. Parameter uncertainties were compared with the Wilcoxon signed rank test. Reproducibility was assessed by using the coefficient of variation. Correlation with histologic findings was evaluated with the Pearson correlation coefficient.

Results: The mean relative fit uncertainty (±standard error) for K^{trans} was 10% ± 1 with the Patlak model, which was significantly lower than that with the Tofts (20% ± 1), extended Tofts (33% ± 3), and extended graphical (29% ± 3) models ($P < .001$). The relative uncertainty for v_p was 20% ± 2 with the Patlak model and was significantly higher with the extended Tofts (46% ± 9) and extended graphical (35% ± 5) models ($P < .001$). The reproducibility (coefficient of variation) for the Patlak model was 16% for K^{trans} and 26% for v_p. Significant positive correlations were found between K^{trans} and the endothelial microvessel content determined on histologic slices (Pearson $\rho = 0.72$, $P = .005$).

Conclusion: The Patlak model is most suited for describing carotid plaque enhancement. Correlation with histologic findings validated K^{trans} as an indicator of plaque microvasculature, and the reproducibility of K^{trans} was good.

[1] From the Department of Radiology (M.E.G., W.H.B., S.R., M.L., S.N.S., K.J., J.E.W., R.M.K., M.E.K.), Cardiovascular Research Institute Maastricht (M.E.G., W.H.B., J.C.S., S.H., M.J.A.P.D., J.E.W., M.E.K.), Department of Pathology (J.P.M.C., J.C.S., S.H., M.J.A.P.D.), and Department of Surgery (J.W.H.D.), Maastricht University Medical Center, P.O. Box 5800, 6202 AZ Maastricht, the Netherlands; School for Mental Health and Neuroscience, Maastricht University, Maastricht, the Netherlands (W.H.B.); and Department of Surgery, Atrium Medical Centre Parkstad, Heerlen, the Netherlands (R.J.T.J.W.). Received March 1, 2012; revision requested April 9; revision received June 28; accepted July 10; final version accepted July 17. This research was performed within the framework of CTMM, the Center for Translational Molecular Medicine (www.ctmm.nl), project PARISk (grant 01C-202), and supported by the Netherlands Heart Foundation. **Address correspondence to** M.E.K. (e-mail: *eline.kooi@mumc.nl*).

Annually, 15 million people worldwide suffer from a stroke, resulting in 5 million deaths and leaving 5 million patients permanently disabled (1). Carotid atherosclerosis is an important cause of stroke. The current treatment strategy for patients with carotid atherosclerosis is based on the degree of stenosis and the presence of clinical symptoms. Large trials have shown that carotid endarterectomy (CEA) is highly beneficial for reducing the risk of recurrent stroke in symptomatic patients with 70%–99% stenosis and marginally beneficial in symptomatic patients with ipsilateral 50%–99% carotid stenosis (2). Although most of these patients will remain event-free without surgery, a considerable number of patients who are currently not scheduled for CEA will experience a recurrent stroke. This indicates that the degree of stenosis is a poor predictor for future ischemic events. Improved risk stratification beyond the degree of stenosis is thus of great importance.

Vulnerable carotid atherosclerotic plaques are likely to cause ischemic cerebrovascular events (3). An important characteristic of vulnerable plaques is increased macrophage content (4). A high rate of oxygen consumption by plaque macrophages causes hypoxia within the plaque, which is a trigger to increase plaque microvasculature (5). Erythrocytes can enter the plaque through these newly formed leaky microvessels, and this is thought to cause intraplaque hemorrhage and subsequent plaque destabilization (6,7). Microvessel density and permeability can be determined noninvasively with dynamic contrast material–enhanced magnetic resonance (MR) imaging (8–11). In dynamic contrast-enhanced MR imaging, the tissue enhancement–time curve after intravenous injection of a bolus of contrast material is measured to estimate pharmacokinetic parameters that describe the blood plasma fraction (v_p), extracellular extravascular volume fraction (v_e), and volume transfer constant (K^{trans}), which reflects microvascular flow, permeability, and surface area. Kerwin and colleagues (8–10) performed several dynamic contrast-enhanced MR imaging studies in carotid atherosclerotic plaques and showed correlations between K^{trans} and v_p and microvessel density and macrophage content.

The choice of the pharmacokinetic model has a large effect on the accuracy and precision of pharmacokinetic parameter estimation for dynamic contrast-enhanced MR imaging. It has been shown that choosing the wrong model can lead to large errors in parameter estimation (12). Although Chen et al (13) performed a model comparison based mainly on simulated data, finding the optimal model for dynamic contrast-enhanced MR imaging data of atherosclerotic plaque has not been explored. In addition, reproducibility has yet to be investigated because it is essential for monitoring disease progression and for reliably estimating pharmacokinetic parameters. The purpose of the present study was to compare four known pharmacokinetic models for their ability to describe dynamic contrast-enhanced MR imaging of carotid atherosclerotic plaques, to determine reproducibility, and to validate the results with histologic findings.

Advances in Knowledge

- The volume transfer constant K^{trans} in carotid atherosclerotic plaques can be reproducibly determined, with a coefficient of variation of 16%.
- The volume transfer constant K^{trans} showed a positive correlation with the endothelial microvessel content in histologic slices obtained in patients who underwent carotid endarterectomy (Pearson ρ = 0.72, P = .005).
- The Patlak model is most suited to describe dynamic contrast material–enhanced MR imaging of carotid plaques and is preferable to the Tofts, extended Tofts, and extended graphical models for the protocol used.

Implication for Patient Care

- K^{trans} is a promising parameter with which to identify patients with vulnerable atherosclerotic plaques with increased microvasculature who might benefit from more aggressive treatment (eg, carotid endarterectomy).

Materials and Methods

Experimental Methods

Study population.—The study was approved by the institutional medical ethics committee. Written informed consent was obtained from all patients. For this prospective study, 29 patients (16 asymptomatic, 13 symptomatic) with 30%–69% carotid stenosis (20 men, nine women; mean age ± standard deviation, 69.3 years ± 6.4) and 16 symptomatic patients with 50%–99% stenosis scheduled for CEA (14 men, two women; mean age, 68.9 years ± 7.6) were included between September 2008 and January 2010. Stenosis grades were measured with ultrasonography (14,15). Exclusion criteria were standard contraindications to MR imaging and a renal clearance of less than 30 mL/min/1.73 m^2. Symptomatic patients had recently (<3 months) experienced

Published online before print
10.1148/radiol.12120499 **Content code:** NR

Radiology 2013; 266:271–279

Abbreviations:
CEA = carotid endarterectomy
ICC = intraclass correlation coefficient
K^{trans} = volume transfer constant
v_e = extracellular extravascular volume fraction
VIF = vascular input function
v_p = blood plasma fraction

Author contributions:
Guarantor of integrity of entire study, M.E.K.; study concepts/study design or data acquisition or data analysis/interpretation, all authors; manuscript drafting or manuscript revision for important intellectual content, all authors; manuscript final version approval, all authors; literature research, M.E.G., S.R., S.N.S., K.J., J.P.M.C., S.H., R.J.T.J.W., J.E.W., M.E.K.; clinical studies, W.H.B., S.R., R.J.T.J.W., J.W.H.D.; experimental studies, M.L., J.P.M.C., J.C.S., R.J.T.J.W.; statistical analysis, M.E.G., S.R., M.L., S.N.S., K.J., R.J.T.J.W.; and manuscript editing, M.E.G., S.R., J.P.M.C., J.C.S., S.H., M.J.A.P.D., R.J.T.J.W., J.E.W., M.E.K.

Conflicts of interest are listed at the end of this article.

amaurosis fugax, transient ischemic attack, or minor stroke. Patients undergoing CEA were selected by a vascular neurologist and a vascular surgeon on the basis of stenosis grade, presence of symptoms, time from the last symptomatic event, and sex (16,17). Surgical specimens were collected from these patients during CEA. Sixteen patients (14 men, two women; mean age, 68.4 years ± 5.4) underwent imaging twice, with a mean of 4.3 days ± 2.8 between examinations, to determine reproducibility.

MR imaging protocol.—MR imaging was performed with a 1.5-T whole-body system (Intera 11.1.4.4; Philips Healthcare, Best, the Netherlands), as previously described (18). A dedicated 47-mm-diameter surface coil (Philips Healthcare) was fixed to the skin at the level of the symptomatic carotid bifurcation. First, the carotid bifurcation was identified with a scout image. The subsequent MR images were centered around the bifurcation. Five MR pulse sequences were used to facilitate delineation of plaque boundaries: *(a)* a three-dimensional T1-weighted turbo field-echo sequence, *(b)* a three-dimensional time-of-flight sequence, *(c)* a multisection T2-weighted turbo spin-echo sequence, and *(d)* unenhanced and *(e)* contrast material–enhanced two-dimensional T1-weighted turbo spin-echo sequences (double inversion-recovery sequence). The contrast-enhanced T1-weighted turbo spin-echo sequence was performed approximately 7 minutes after injection of 0.1 mmol per kilogram body weight gadopentetate dimeglumine (Magnevist; Bayer Schering Pharma, Berlin, Germany). The field of view was 100 × 80 mm, and the matrix size was 256 × 163–205.

Dynamic contrast-enhanced MR imaging was performed between acquisition of pre- and postcontrast T1-weighted turbo spin-echo images. The optimal gate delay and width with minimal flow were determined for each patient from phase-contrast quantitative flow measurements by using electrocardiographic triggering. Three-dimensional dynamic contrast-enhanced T1-weighted fast field-echo images were acquired by obtaining 10 transverse over-contiguous sections for 16 time frames with a typical separation of 25 seconds (depending on gate width) between frames. Total imaging time was approximately 7 minutes. Contrast material was intravenously injected at the beginning of the third time frame with use of a power injector (Spectris Solaris; Medrad, Warrendale, Pa). Contrast material was injected at a rate of 0.5 mL/sec, followed by injection of a 20-mL saline flush at the same rate. Relevant imaging parameters were as follows: repetition time msec/echo time msec, 12/3; flip angle, 35°; image percentage, 75%; number of signals acquired, one; section thickness, 6.0 mm; overlap, 3.0 mm; field of view, 100 × 100 mm; and matrix size, 256 × 256. For the patients who underwent CEA, section thickness was decreased to 3.0 mm with an overlap of 1.5 mm and the matrix size was 160 × 160. In addition, a spatial saturation slab at the caudal position parallel to the imaging plane was added to reduce inflow artifacts. For three additional patients with 30%–69% carotid stenosis, higher temporal resolution dynamic contrast-enhanced MR images (sample time, 6 seconds) were acquired with parameters that were identical to those used for the patients who did not undergo surgery, except for matrix size, which was decreased to 64 × 64.

Image review.—Lumen and outer plaque contours were drawn manually by one reader (R.M.K., with 2 years of experience in plaque analysis with MR imaging) with use of dedicated vessel wall analysis software (VesselMASS; Department of Radiology, Leiden University Medical Center, Leiden, the Netherlands). Lumen contours were drawn on time-of-flight images. Care was taken to avoid voxels with partial volume effects. Outer plaque contours were drawn by using a combination of T1-weighted turbo field-echo, T2-weighted turbo spin-echo, and pre- and postcontrast T1-weighted turbo spin-echo images, as described previously (18–21). Those contours were copied to the dynamic images. Dynamic contrast-enhanced MR images were shifted manually to correct for small patient movements. Outer plaque contours were corrected to include the adventitial vasa vasorum, which shows hyperenhancement after contrast material administration (Fig 1).

Histologic and immunohistochemistry examinations.—Carotid artery specimens were removed during surgery and cut into 3-mm-thick slices, after which they were fixed in formalin for 24 hours. Then, samples were decalcified, processed, embedded in paraffin,

Figure 1

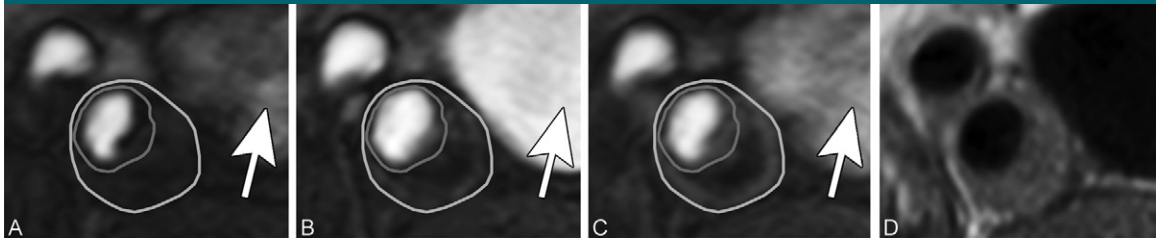

Figure 1: *A–C*, Dynamic contrast-enhanced MR images obtained, *A*, before contrast material administration, *B*, 2 minutes after injection, and *C*, 6 minutes after injection. Arrow = jugular vein. *D*, T1-weighted turbo field-echo image for anatomic reference. Tissue response function is determined in region between outer plaque contour and inner lumen contour in the carotid internal artery.

cut into 4-μm-thick (transverse) slices, and stained with hematoxylin-eosin. Plaque microvasculature was detected with immunohistochemistry by using a cocktail of primary antibodies against CD31 (1:40 clone JC70A; Dako North America, Carpinteria, Calif) and CD34 (1:200 clone Qbend; Monosan, Uden, the Netherlands).

Cross-sections were deparaffinized and dehydrated. For antigen retrieval, slides were heated in Tris-HCl with 1 mmol/L ethylenediaminetetraacetic acid (pH, 8) in a microwave. Slices were incubated with the CD31-CD34 cocktail and subsequently exposed to peroxidase-conjugated secondary immunoglobulins. Peroxidase activity was visualized by using Vector red alkaline phosphatase substrate (Vector Laboratories, Burlingame, Calif) as a chromogen. Slices were counterstained with hematoxylin. Slices incubated without the primary antibody served as negative control and showed no staining.

The histologic slices were coregistered to MR imaging sections on the basis of their longitudinal position relative to the carotid bifurcation. Matching between MR images and histologic slices was verified by comparing plaque morphology and composition (eg, calcifications, intraplaque hemorrhage) of coregistered MR images and histologic slices (R.M.K., with 2 years of experience with plaque analysis). Coregistered MR images and histologic slices that showed no correspondence in plaque morphology or composition were excluded from further data analysis. Plaque microvasculature was assessed on high-spatial-resolution digital images by using morphometric analysis software (QWin V3; Leica, Cambridge, England). The endothelial microvessel area was measured as the cross-sectional CD31-CD34–positive area surrounding a microvessel lumen (M.E.G., with 1 year of experience with immunohistochemical analysis, under supervision of J.C.S., with 10 years of experience with immunohistochemical analysis). Total endothelial microvessel content was calculated by dividing the endothelial microvessel area by the total tissue cross-sectional area.

Pharmacokinetic Modeling

For the estimation of the pharmacokinetic parameters, we used a two-compartment model previously described by Tofts et al (22,23). The model consists of a plasma compartment and the extracellular extravascular space. Various pharmacokinetic models have been developed that solve this two-compartment model under certain assumptions. The four models that we compared in the present study are described in Table 1.

Data Analysis

Mean plaque enhancement.—Analysis of mean plaque enhancement was performed on two subsequent sections with maximum plaque thickness for the nonsurgery patients and on all even-numbered sections for the patients who underwent CEA. Briefly, gadolinium concentrations were determined from the signal intensity time courses by using the Ernst equation (25), the $r1$ and $r2$ relaxivities, and literature values for T_{10} and T_{20} (the T1 and T2 relaxation times of the tissue in the absence of any contrast material) (26).

Curve fitting for the experimental data was performed by using the least-squares curve-fitting routine lsqcurvefit (Matlab; Mathworks, Natick, Mass) with Gauss-Newton optimization. To exclude nonphysical solutions, the parameters v_e and v_p were constrained to a maximum of 1. Model comparison was performed by averaging the concentration between outer plaque and lumen contours and then fitting the pharmacokinetic model (region of interest–based fitting). In addition, the concentration-time curves were fitted for each vessel wall voxel separately (voxel-wise fitting). This enables generation of K^{trans} maps with which to assess plaque heterogeneity. Then, the resulting pharmacokinetic parameters were averaged over all voxels.

Vascular input function.—A general vascular input function (VIF) (27,28) was determined from moderate-temporal-resolution images (n = 3) with a temporal resolution of 6 seconds. The VIF was determined from a 3-mm-diameter circular region of interest in the center of the jugular vein at the most caudal section. For each high-temporal-resolution VIF, a fit was performed with use of a slightly adapted equation introduced by Parker et al (27), as follows:

$$C_p(t) = \frac{A}{\sigma\sqrt{2\pi}} e^{\frac{-(t-T)^2}{2\sigma^2}} + \frac{\alpha e^{-\beta t}}{1+e^{-s(t-\tau)}},$$

where A, σ, and T are the scaling constant, width, and center of the Gaussian, respectively; α and β the amplitude and decay constant of the exponential function, respectively; and s and τ the width and center of the sigmoid, respectively. The Parker formula uses a mixture of two Gaussian functions to describe the first and second pass peak of contrast material. Because the second pass peak could not be detected in the present high-temporal-resolution data, one Gaussian function was sufficient to describe the VIF (Fig 2). The VIF used for data analysis was constructed from the average parameters of the three high-temporal-resolution images. The VIF was shifted automatically to align the bolus start with the moment of contrast material administration (beginning of third time point) for each patient individually.

Determination of model of preference.—Relative fit errors (*RFE*) were calculated for the entire patient population. Fit errors indicate the ability of each model to describe the data and are calculated as follows:

$$RFE = \sqrt{\frac{\sum (C_{t,fit} - C_t)^2}{\sum C_t^2}} \cdot 100\%,$$

where $C_{t,fit}$ is the fitted tissue concentration and C_t the measured tissue concentration at the sampled time points.

The precision at which the model is able to measure pharmacokinetic parameters was examined quantitatively. The relative estimation uncertainties for K^{trans}, v_e, and v_p were calculated by using the diagonal elements of the covariance matrix and normalizing to the estimated pharmacokinetic parameters for each fit.

F tests were performed to find the model that best fitted the data. Initially, the two-parameter models and

Table 1

Description of Pharmacokinetic Two-Compartment Model and Model Solutions

Parameter	Mathematic Description	Parameters
Two-compartment model	$\frac{dC_e(t)}{dt} = \frac{K^{trans}}{v_e}[C_p(t) - C_e(t)]$	
	$C_t(t) = v_p C_p(t) + v_e C_e(t)$	
	…	
Model solutions		
Tofts (22,23)	$C_t(t) = K^{trans}\int_0^t C_p(\tau)e^{\frac{K^{trans}}{v_e}(\tau - t)}d\tau$	K^{trans}, v_e
Extended Tofts (22,23)	$C_t(t) = v_p C_p(t) + K^{trans}\int_0^t C_p(\tau)e^{\frac{K^{trans}}{v_e}(\tau - t)}d\tau$	K^{trans}, v_e, v_p
Patlak (24)	$C_t(t) = v_p C_p(t) + K^{trans}\int_0^t C_p(\tau)d\tau$	K^{trans}, v_p
Extended graphical (13)	$C_t(t) = v_p C_p(t) + K^{trans}\int_0^t C_p(\tau)d\tau - \frac{K^{trans^2}}{v_e}\int_0^t\int_0^{\tau_1} C_p(\tau_2)d\tau_2 d\tau_1$	K^{trans}, v_e, v_p

Note.—$C_e(t)$ = extracellular extravascular space contrast material concentration, $C_p(t)$ = blood plasma contrast material concentration, $C_t(t)$ = total tissue contrast material concentration.

Figure 2

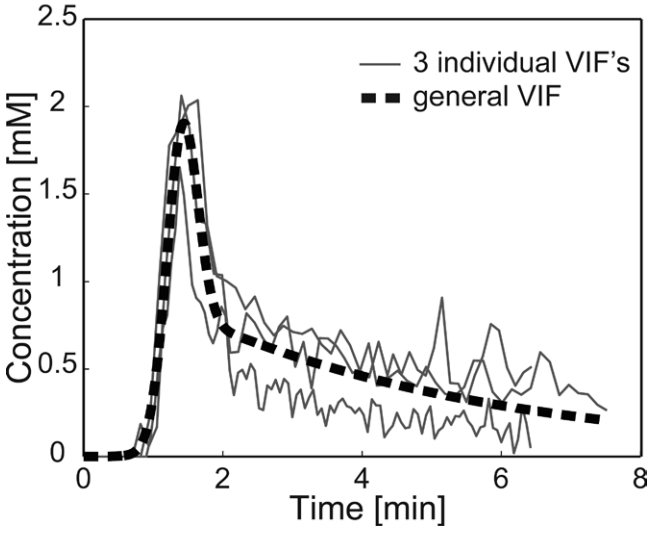

Figure 2: General VIF (dashed line) determined from three individual VIFs (solid lines) in a region of interest in jugular vein on three high-temporal-resolution images. For each high-temporal-resolution VIF, a fit was performed by using a slightly adapted formula introduced by Parker et al (27). Mean parameters used to construct the general VIF were as follows: scaling constant of Gaussian = 0.82 mmol · min, center of Gaussian = 1.40 minutes, width of Gaussian = 0.22 minutes, amplitude = 1.14 mmol, decay constant = 0.23 min^{-1}, width of sigmoid = 6.67 min^{-1}, and center of sigmoid = 1.41 minutes.

three-parameter models were compared separately to determine which model was better with regard to the relative fit errors. Subsequently, it was investigated whether the expansion to the best three-parameter model brought an improvement. For this, the *F* statistic was calculated according to the extra sum of squares method, as follows:

$$F_{df_3 - df_2} = \frac{(SS_2 - SS_3)/(df_2 - df_3)}{SS_3/df_3},$$

where $SS_n = \Sigma(C_{t,fitn} - C_t)^2$ is the sum of squares and df_n is the degrees of freedom for the model with *n* parameters.

Uncertainties in the estimation of pharmacokinetic parameters were compared by using the paired Wilcoxon signed rank test with Bonferroni correction for K^{trans}, v_e, and v_p.

The pharmacokinetic parameters provided by the different models were compared by calculating the mean relative differences and the Pearson correlation coefficient. $P < .05$ (two-tailed) was indicative of a significant difference.

Reproducibility.—Reproducibility was assessed for all pharmacokinetic models by using voxel-wise fitting. Mean plaque pharmacokinetic parameters were evaluated with Bland-Altman plots (29,30). Reproducibility was assessed quantitatively by using the intraclass correlation coefficient (ICC) (one-way random, single measures) and the coefficient of variation. K^{trans} maps were compared qualitatively to assess whether the general spatial distribution of K^{trans} values could be reproduced.

Correlation with histologic findings.—K^{trans} values and endothelial microvessel content were averaged on plaque level. Correlation between the resulting K^{trans} values and the endothelial microvessel content was investigated by using the Pearson correlation coefficient.

Results

General VIF

Figure 2 shows the general VIF based on the three fitted high-temporal-resolution VIFs.

Relative Fit Error and Parameter Uncertainties for the Various Models

Of the 45 patients originally included in this study, two had to be excluded because of insufficient MR image quality caused by severe patient movement. Thus, data from 43 patients were analyzed to determine the model of preference (Table 2).

When we looked at relative fit errors of the two-parameter models, the Patlak model was found to fit the data better than the Tofts model in 35 of the 43 patients ($P < .05$ for 12 patients). Because there was not one case for which the Tofts model was significantly better than the Patlak model, it was concluded that the Patlak model was the best of the two-parameter models. Looking at the tissue concentration–time curves (Fig 3), this was to be expected because the Tofts model is not able to model the first pass peak of the contrast material. Between the three-parameter models, the extended Tofts model had lower relative fit errors than the extended graphical model for 37 of the 43 patients. However, these differences were only significant in two patients. Expansion from the Patlak to the extended Tofts model brought a significant improvement in fit quality for only 10 of the 43 patients ($P < .05$), whereas a deterioration was observed in 18.

The Patlak model had a significantly lower uncertainty in K^{trans} and v_p compared with the other models ($P < .001$). Because of the additional parameter, the three-parameter models suffer from higher parameter uncertainties. In particular, the estimation uncertainties in v_e were very high, that is, mean relative uncertainties were more than 100%.

Comparison of Pharmacokinetic Parameters

The pharmacokinetic parameters estimated with the extended Tofts, Patlak, and extended graphical models showed very strong correlations (Pearson $\rho > 0.95$ in the pairwise comparisons, $P < .001$). Correlation of those parameters estimated with the Tofts model versus the other models were moderate (Pearson $\rho = 0.64$–0.66) but still highly significant ($P < .001$). The differences in the mean pharmacokinetic parameters for the extended Tofts and extended graphical models were 4% for K^{trans} and less than 10% for v_e and v_p. Relative to the extended Tofts model, the mean K^{trans} value was 16% higher for the Tofts model and 27% lower for the Patlak model. The mean value for v_p obtained with the Patlak model was 22% higher than that with the extended Tofts model, and the mean value for v_e obtained with the Tofts model was 36% lower. Because the true pharmacokinetic parameters are unknown, absolute validation is impossible.

Table 2

Relative Fit Errors and Fit Uncertainties for the Four Models

Parameter	Tofts Model	Extended Tofts Model	Patlak Model	Extended Graphical Model
Relative fit error (%)	26 ± 2	19 ± 1	20 ± 1	20 ± 1
Uncertainty (%)				
K^{trans}	20 ± 1	33 ± 3	10 ± 1	29 ± 3
v_e	22 ± 2	(2 ± 1) · 10^3	…	(1 ± 3) · 10^2
v_p	…	46 ± 9	20 ± 2	35 ± 5

Note.—Data are means ± standard errors. Note that v_p and v_e are not included in the Tofts and Patlak models, respectively.

Figure 3

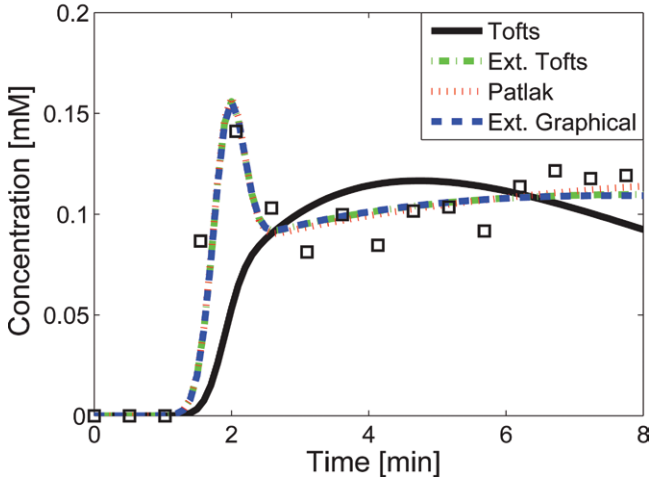

Figure 3: Example of plaque concentration–time curve with fits for the four different models. The Tofts model neglects the vascular term and cannot model the first pass peak, which is clearly visible in experimental data (□). *Ext.* = extended.

Reproducibility

The reproducibility for K^{trans} was good for all considered pharmacokinetic models (ICC > 0.6; $P < .05$). The ICC was largest for the Patlak model (ICC = 0.79). Significant ICCs for the parameters v_e and v_p could only be found for the Tofts and Patlak models, respectively (Table 3). The ICC for v_p is largely influenced by one outlier in the data set. When excluding that patient, values largely improved. Bland-Altman plots (not shown) demonstrated that the within-subject difference was not dependent on the mean parameter values.

Qualitative evaluation of K^{trans} maps showed global similarities in the K^{trans}

Table 3

Reproducibility of Mean Voxel Pharmacokinetic Parameters

	ICC			Coefficient of Variation (%)		
Model	K^{trans}	v_p	v_e	K^{trans}	v_p	v_e
Tofts	0.62*	…	0.48*	15	…	11
Extended Tofts	0.65*	0.14 (0.17)	0.32	18	44 (40)	12
Patlak	0.79*	0.48* (0.65*)	…	16	26 (19)	…
Extended graphical	0.71*	0.38 (0.53*)	0.27	13	33 (24)	9

Note.—Values in parentheses were obtained after the exclusion of one outlier.

* Statistically significant ($P < .05$).

Figure 4

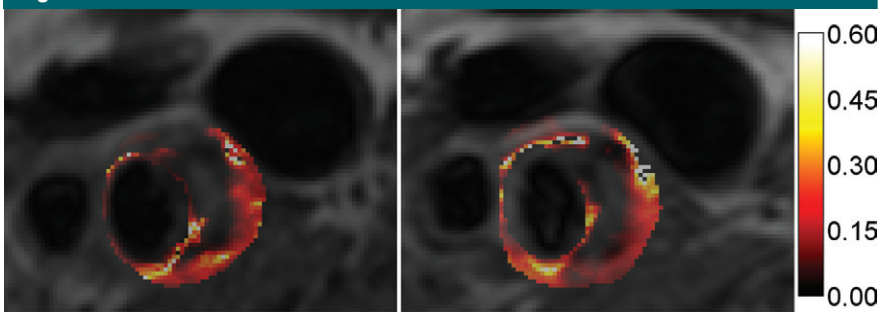

Figure 4: K^{trans} maps in 70-year-old man. Maps were generated from images obtained 1 week apart. Parametric maps are overlaid on anatomic MR images, and voxel K^{trans} values (Patlak model) are color coded from 0 to 0.6 min^{-1}. The necrotic core exhibiting low K^{trans} values at center of plaque, the highly vascularized adventitia at outer rim with high K^{trans} values, and another region of higher K^{trans} values near inner rim of plaque are clearly reproduced on both images.

Table 4

Correlation of K^{trans} with Endothelial Microvessel Content for the Four Models

	Voxel-wise Fitting		Region of Interest–based Fitting	
Model	Pearson ρ	*P* Value	Pearson ρ	*P* Value
Tofts	0.31	.303	0.02	.941
Extended Tofts	0.47	.109	0.74*	.004
Patlak	0.72*	.005	0.70*	.008
Extended graphical	0.65*	.015	0.69*	.009

* Statistically significant correlation.

distribution between the images obtained on different days (Fig 4).

Correlation with Histologic Findings

Of the 16 patients in whom plaque specimens were acquired, one had to be excluded because of insufficient MR image quality. For another two patients, the histologic slices could not be coregistered reliably to MR images. In the end, a total of 52 slices from 13 patients could be analyzed for correlation with histologic findings. K^{trans} showed significant correlation ($P < .01$) with the mean endothelial microvessel content for all models except the Tofts model using region of interest–based fitting (Table 4).

Discussion

In the current study, using relative fit errors and uncertainties as criteria, we found that as compared with the Tofts, extended Tofts (22,23), and extended graphical models (13), the Patlak model (24) is most suited to describe dynamic contrast-enhanced MR imaging of carotid plaques. Fit error analysis showed that the Tofts model lacked sufficient parameters for describing plaque enhancement. This result is a reflection of the inability of this model to describe the first-pass plasma peak present in the concentration-time curves. The extended Tofts and extended graphical models both provided good fits to the data, but, when looking at fit uncertainties, it was clear that v_e could not be estimated reliably, which is also reflected in low K^{trans} precision because these parameters are interdependent (31). This may also explain the differences in absolute values of K^{trans} when introducing additional pharmacokinetic parameters, which is in agreement with previous findings (32). Consequently, fit uncertainties for the three-parameter models were too high to obtain reliable results.

The estimation of v_e is largely influenced by the total imaging period because it depends on whether significant reflux is present in the tissue response function. The measured curves showed little or no reflux of contrast material for acquisition times of up to 7 minutes, which explains the low precision for v_e. Longer acquisition times would likely improve precision for v_e estimates (33) but are impractical for a clinical application. The reproducibility was better for K^{trans} than for v_p and v_e, which could only be reproducibly determined with the respective two-parameter models. This is in line with the higher parameter estimation uncertainties for the three-parameter models.

Strong correlation of K^{trans} values with the endothelial microvessel content in histologic slices confirmed that dynamic contrast-enhanced MR imaging is a highly adequate technique with which to assess plaque microvasculature, which is in line with findings

from previous studies (8,9). The fact that no correlation was found for the Tofts model is not surprising because it was not able to accurately describe the plaque enhancement. The poor correlation for the extended Tofts model using voxel-wise fitting indicates that this model is too complex to be reliably used for voxel-wise fitting. In our study, validation of the parameter v_p was not feasible because rapid extravasation of the contrast material hindered its accurate estimation.

The amount of plaque microvasculature is thought to be a key aspect of plaque vulnerability (6,7). The information provided by K^{trans} is thus promising to identify patients with vulnerable atherosclerotic plaques who might benefit from more aggressive treatment, such as CEA. Furthermore, dynamic contrast-enhanced MR imaging could provide valuable information in the assessment of novel drug therapies intended to prevent plaque angiogenesis and, thus, plaque destabilization.

Previously, injection rates for dynamic contrast-enhanced MR imaging of atherosclerotic plaques of 2 mL/sec have been used (8–10). Because the K^{trans} of the vessel wall was expected to be less than 0.2 min^{-1}, we used a slow injection rate (0.5 mL/sec), which weakens the requirement of a high temporal resolution and thus provides a possibility to increase the spatial resolution, which is required for a vessel wall. Previously, Aerts et al (34) showed that a higher injection rate is most beneficial for high K^{trans} values (>0.2 min^{-1}), whereas, for low values (<0.2 min^{-1}), the errors in K^{trans} estimation are much smaller and the injection rate is less critical.

In contrast to our results, Chen et al (13) found their extended graphical model to have some advantages over the Patlak model, both for simulated data and selected in vivo data of carotid plaques with good to excellent image quality. The differing conclusions might be attributed to differences in the experimental protocols (eg, injection rate). Their results show that in the choice between the Patlak and extended graphical model a compromise between sensitivity to bias and noise must be made. In our study, the high parameter uncertainties for the extended graphical model and the absence of reflux in the tissue response function speak in favor of the Patlak model.

Our study has some limitations. Validation of our approach with histologic data was only feasible for patients who underwent CEA. Thus, the correlation with the endothelial microvessel content could only be demonstrated for symptomatic patients with presumably vulnerable plaques and not for the whole patient population. Another limitation is the low temporal resolution of our data, which had to be sacrificed for the high spatial resolution needed for vessel wall imaging. Technical improvements leading to a better temporal resolution would improve parameter estimation, especially with regard to v_p. Furthermore, the initial section thickness was relatively large (6 mm). It was reduced to 3 mm for the patients who underwent CEA owing to advancement of knowledge during the study, improving spatial localization.

The Patlak model is more suitable than the Tofts, extended Tofts, and extended graphical models for describing the presented dynamic contrast-enhanced MR imaging data of atherosclerotic plaques in a clinical setting, and the parameter K^{trans} provides valuable information about the plaque microvasculature and can be reproducibly determined. Prospective clinical studies are warranted to assess the value of dynamic contrast-enhanced MR imaging in the prediction of cerebrovascular ischemic events.

Acknowledgments: The authors thank Raf van Hoof, MSc (Department of Radiology, Maastricht University Medical Center), for his help with data processing and Anique Janssen-Vrehen, BSc, and Clairy Dinjens, MD (Department of Pathology, Maastricht University Medical Center), for histologic processing.

Disclosures of Conflicts of Interest: M.E.G. Financial activities related to the present article: institution received a grant from the Center for Translational Molecular Medicine. Financial activities not related to the present article: none to disclose. Other relationships: none to disclose. **W.H.B.** Financial activities related to the present article: institution received a grant from the Center for Translational Molecular Medicine. Financial activities not related to the present article: none to disclose. Other relationships: none to disclose. **S.R.** No conflicts of interest to disclose. **M.L.** No relevant conflicts of interest to disclose. **S.N.S.** Financial activities related to the present article: institution received a grant from the Center for Translational Molecular Medicine. Financial activities not related to the present article: none to disclose. Other relationships: none to disclose. **K.J.** No relevant conflicts of interest to disclose. **J.P.M.C.** Financial activities related to the present article: institution received a grant from the Center for Translational Molecular Medicine. Financial activities not related to the present article: none to disclose. Other relationships: none to disclose. **J.C.S.** Financial activities related to the present article: institution received a grant from the Center for Translational Molecular Medicine. Financial activities not related to the present article: none to disclose. Other relationships: none to disclose. **S.H.** Financial activities related to the present article: institution received a grant from the Center for Translational Molecular Medicine. Financial activities not related to the present article: none to disclose. Other relationships: none to disclose. **M.J.A.P.D.** Financial activities related to the present article: institution received a grant from the Center for Translational Molecular Medicine. Financial activities not related to the present article: none to disclose. Other relationships: none to disclose. **R.J.T.J.W.** No relevant conflicts of interest to disclose. **J.W.H.D.** No relevant conflicts of interest to disclose. **J.E.W.** Financial activities related to the present article: none to disclose. Financial activities not related to the present article: institution has a grant or grant pending with Siemens, Philips, GE Healthcare, Bracco, and Bayer; receives payment for lectures including service on speakers bureaus from Siemens, GE Healthcare, Bayer, and Boston Scientific; institution receives payment for lectures including speakers bureaus from Siemens, GE Healthcare, Bayer, and Boston Scientific; receives payment for development of educational presentations from Bayer. Other relationships: none to disclose. **R.M.K.** No relevant conflicts of interest to disclose. **M.E.K.** Financial activities related to the present article: institution received a grant from the Center for Translational Molecular Medicine. Financial activities not related to the present article: none to disclose. Other relationships: none to disclose.

References

1. Mackay J, Mensah GA. Atlas of heart disease and stroke. Geneva, Switzerland: World Health Organization, 2004.
2. Chaturvedi S, Bruno A, Feasby T, et al. Carotid endarterectomy: an evidence-based review— report of the Therapeutics and Technology Assessment Subcommittee of the American Academy of Neurology. Neurology 2005;65(6):794–801.

3. Naghavi M, Libby P, Falk E, et al. From vulnerable plaque to vulnerable patient: a call for new definitions and risk assessment strategies: part II. Circulation 2003;108(15):1772–1778.

4. Ross R. Atherosclerosis: an inflammatory disease. N Engl J Med 1999;340(2):115–126.

5. Sluimer JC, Gasc JM, van Wanroij JL, et al. Hypoxia, hypoxia-inducible transcription factor, and macrophages in human atherosclerotic plaques are correlated with intraplaque angiogenesis. J Am Coll Cardiol 2008;51(13):1258–1265.

6. Virmani R, Kolodgie FD, Burke AP, et al. Atherosclerotic plaque progression and vulnerability to rupture: angiogenesis as a source of intraplaque hemorrhage. Arterioscler Thromb Vasc Biol 2005;25(10):2054–2061.

7. Kolodgie FD, Gold HK, Burke AP, et al. Intraplaque hemorrhage and progression of coronary atheroma. N Engl J Med 2003;349(24):2316–2325.

8. Kerwin W, Hooker A, Spilker M, et al. Quantitative magnetic resonance imaging analysis of neovasculature volume in carotid atherosclerotic plaque. Circulation 2003;107(6):851–856.

9. Kerwin WS, O'Brien KD, Ferguson MS, Polissar N, Hatsukami TS, Yuan C. Inflammation in carotid atherosclerotic plaque: a dynamic contrast-enhanced MR imaging study. Radiology 2006;241(2):459–468.

10. Kerwin WS, Oikawa M, Yuan C, Jarvik GP, Hatsukami TS. MR imaging of adventitial vasa vasorum in carotid atherosclerosis. Magn Reson Med 2008;59(3):507–514.

11. Calcagno C, Mani V, Ramachandran S, Fayad ZA. Dynamic contrast enhanced (DCE) magnetic resonance imaging (MRI) of atherosclerotic plaque angiogenesis. Angiogenesis 2010;13(2):87–99.

12. Buckley DL. Uncertainty in the analysis of tracer kinetics using dynamic contrast-enhanced T1-weighted MRI. Magn Reson Med 2002;47(3):601–606.

13. Chen H, Li F, Zhao X, Yuan C, Rutt B, Kerwin WS. Extended graphical model for analysis of dynamic contrast-enhanced MRI. Magn Reson Med 2011;66(3):868–878.

14. Grant EG, Benson CB, Moneta GL, et al. Carotid artery stenosis: gray-scale and Doppler US diagnosis—Society of Radiologists in Ultrasound Consensus Conference. Radiology 2003;229(2):340–346.

15. Kwee RM, van Oostenbrugge RJ, Prins MH, et al. Symptomatic patients with mild and moderate carotid stenosis: plaque features at MRI and association with cardiovascular risk factors and statin use. Stroke 2010;41(7):1389–1393.

16. Rothwell PM, Eliasziw M, Gutnikov SA, et al. Analysis of pooled data from the randomised controlled trials of endarterectomy for symptomatic carotid stenosis. Lancet 2003;361(9352):107–116.

17. Rothwell PM, Eliasziw M, Gutnikov SA, Warlow CP, Barnett HJ; Carotid Endarterectomy Trialists Collaboration. Endarterectomy for symptomatic carotid stenosis in relation to clinical subgroups and timing of surgery. Lancet 2004;363(9413):915–924.

18. Kwee RM, van Oostenbrugge RJ, Mess WH, et al. Carotid plaques in transient ischemic attack and stroke patients: one-year follow-up study by magnetic resonance imaging. Invest Radiol 2010;45(12):803–809.

19. Kwee RM, Teule GJ, van Oostenbrugge RJ, et al. Multimodality imaging of carotid artery plaques: 18F-fluoro-2-deoxyglucose positron emission tomography, computed tomography, and magnetic resonance imaging. Stroke 2009;40(12):3718–3724.

20. Yuan C, Mitsumori LM, Ferguson MS, et al. In vivo accuracy of multispectral magnetic resonance imaging for identifying lipid-rich necrotic cores and intraplaque hemorrhage in advanced human carotid plaques. Circulation 2001;104(17):2051–2056.

21. Mitsumori LM, Hatsukami TS, Ferguson MS, Kerwin WS, Cai J, Yuan C. In vivo accuracy of multisequence MR imaging for identifying unstable fibrous caps in advanced human carotid plaques. J Magn Reson Imaging 2003;17(4):410–420.

22. Tofts PS. Modeling tracer kinetics in dynamic Gd-DTPA MR imaging. J Magn Reson Imaging 1997;7(1):91–101.

23. Tofts PS, Brix G, Buckley DL, et al. Estimating kinetic parameters from dynamic contrast-enhanced T(1)-weighted MRI of a diffusable tracer: standardized quantities and symbols. J Magn Reson Imaging 1999;10(3):223–232.

24. Patlak CS, Blasberg RG, Fenstermacher JD. Graphical evaluation of blood-to-brain transfer constants from multiple-time uptake data. J Cereb Blood Flow Metab 1983;3(1):1–7.

25. Ernst RR. Application of Fourier transform spectroscopy to magnetic resonance. Rev Sci Instrum 1966;37(1):93.

26. Haacke E, Brown RW, Thompson M, Venkatesan R. Magnetic resonance imaging physical principles and sequence design. New York, NY: Wiley, 1999.

27. Parker GJ, Roberts C, Macdonald A, et al. Experimentally-derived functional form for a population-averaged high-temporal-resolution arterial input function for dynamic contrast-enhanced MRI. Magn Reson Med 2006;56(5):993–1000.

28. Weinmann HJ, Laniado M, Mützel W. Pharmacokinetics of GdDTPA/dimeglumine after intravenous injection into healthy volunteers. Physiol Chem Phys Med NMR 1984;16(2):167–172.

29. Bland JM, Altman DG. Statistical methods for assessing agreement between two methods of clinical measurement. Int J Nurs Stud 2010;47(8):931–936.

30. Bland JM, Altman DG. Measurement error. BMJ 1996;313(7059):744.

31. Lopata RG, Backes WH, van den Bosch PP, van Riel NA. On the identifiability of pharmacokinetic parameters in dynamic contrast-enhanced imaging. Magn Reson Med 2007;58(2):425–429.

32. Jaspers K, Leiner T, Dijkstra P, et al. Optimized pharmacokinetic modeling for the detection of perfusion differences in skeletal muscle with DCE-MRI: effect of contrast agent size. Med Phys 2010;37(11):5746–5755.

33. Jaspers K, Aerts HJ, Leiner T, et al. Reliability of pharmacokinetic parameters: small vs. medium-sized contrast agents. Magn Reson Med 2009;62(3):779–787.

34. Aerts HJ, van Riel NA, Backes WH. System identification theory in pharmacokinetic modeling of dynamic contrast-enhanced MRI: influence of contrast injection. Magn Reson Med 2008;59(5):1111–1119.